

Observing a Central Supermassive Black Hole in Type 1 Seyfert NGC 4151

Uzair Tahamid Siam, Navya Uberoi

January 21, 2022

Abstract

In this project we compare a type-1 Seyfert with another spiral galaxy of the same Hubble type and estimate a lower mass limit of the black hole that is present at the center of the Seyfert galaxy. Through our analysis we find that Seyfert NGC 4151 is a black hole, with a minimum mass of about $10^5 M_\odot$ and a luminosity of around $10^9 L_\odot$ which is about 2 orders of magnitude lower than the current estimates of the mass of this SMBH. We also conclude that although the center seems to be blue, it also has a strong emission line in H α and a weak emission line in [OIII]. The central object is extremely bright, making up for about 25% of the total luminosity of the galaxy, a feature absent in the non-Seyfert spiral NGC 4145.

1 Introduction

Perhaps the most controversial yet fascinating idea to emerge from Einstein's theory of general relativity was regarding the existence of black holes — objects that do not allow even light to escape the influence of their gravity. It was years before these objects were identified and studied, and we have since made great strides in understanding the properties of these mysterious objects. However, it was only in the 1970s that astronomers Bruce Balick and Robert Brown discovered the first signs that the massive object in the center of the Milky Way is indeed a black hole [2]. Soon, it became apparent that virtually every galaxy in the observable universe hosts a supermassive black hole in its center, and has a mass of the order of millions of solar masses.

In 1943, astronomer Carl Seyfert came across a special class of spiral galaxies that are now named after him - Seyfert galaxies [7]. These special spiral galaxies were found to have an extremely bright (about a factor ten times bright than the rest of the galaxy) center, which was later found to be accreting matter, therefore being an "active" nucleus – a feature very rare among spiral galaxies. In addition to being incredibly bright, the active nucleus also contains ionized gas for which the emission-line spectrum indicates an ionization state substantially higher than the typical HII regions associated with star formation. Seyferts can be classified into two broad categories – Type 1 and Type 2. Type 1 Seyferts, which are of interest to us in this project, have broad hydrogen recombination lines due to high Doppler velocities in center with respect to the rest of the galaxy.

In this project we will be imaging a Type-1 Seyfert so we can see deeper towards the center of the black hole, and also a non-Seyfert type spiral galaxy of the same Hubble classification. Using the images of these galaxies our goal is to demonstrate that Seyfert galaxies have a star-like, extremely luminous central object which is lacking in most spiral galaxies of the same Hubble type and then infer certain bounds on central black hole properties.

2 Instrument and Targets

2.1 The Telescope

The telescope used in this project [4] is located in the University of Rochester's C.E.K. Mees Observatory, 40 miles south of Rochester in the Bristol Hills ($77^{\circ}24'31.56''$ W, $42^{\circ}42'01.0''$ N) at an elevation of 701 m (2260 ft). The 24-inch Cassegrain telescope by DFM engineering installed in 1965 has f/13.5, plate scale 25.1 arcsec/mm in the Cassegrain focal plane. The large CCD covers 0.224 arcsec/pixel in 1x1 binning, 15.4 arcmin on a side, 21.7 arcmin diagonal. The autoguider CCD: 0.259 arcsec/pixel, 2.8x2.1 arcmin. It has an unvignetted field of view 24 arcmin in diameter and collecting area: $2700 \text{ cm}^2 = 0.27 \text{ m}^2$.

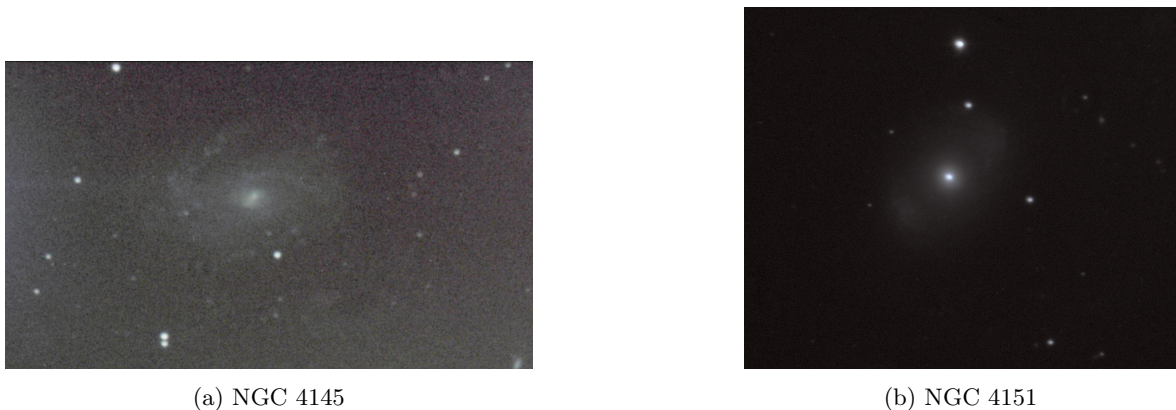
Facility focal-plane instruments include:

- an SBIG STX-16803 CCD camera (4096x4096 pixels, 15.4 arcmin square field of view), with an internal autoguider and a complement of broadband - L, R, G, B which have peak $\tau \geq 0.95$ - and spectral-line filters - [OIII], H α , [SII] all of which have peak $\tau = 0.85 - 0.9$ and FWHM, $\Delta\lambda = 8.5, 7.0, 8.0 \text{ nm}$ respectively.
- a Shelyak LHiRes III grating spectrograph (resolving power up to 18000) with a slit-viewing video camera and an SBIG ST-7 focal-plane camera.

2.2 Target Galaxies and Calibration Star

In this project, we choose to observe two galaxies - NGC 4151 and NGC 4145. NGC 4151 is an intermediate spiral galaxy (SABb) with Type 1 Seyfert classification. It is located 15.8 Mpc away from Earth in the constellation Canes Venatici [8], and has an apparent angular size 6.4x5.5. Located in the same constellation, NGC 4145 is also a spiral galaxy (SABd) located 20 Mpc away from Earth with an apparent size 5.9'x4.1' [9]. This galaxy will act as a reference in our analysis, to which we shall compare the properties of the central bright object in our chosen Seyfert galaxy. These objects were in part chosen because around March 2021, the transit point of these objects were very close to zenith. This not only would give us a chance to observe them throughout the night, but also reduce the effects of atmospheric extinction when observed close to zenith. Since the light from objects close to zenith passes through the least amount of atmosphere, we expect lesser atmospheric extinction and blurring in our images.

The images captured from the CCD camera at the telescope would yield a two dimensional array of pixels, with each pixel containing a value in Data Numbers (DNs). To convert from DNs to physical flux units, we require a calibration object whose flux is known in all the filters we are imaging in. An obvious choice is an A0V star, since its fluxes are well-measured. We choose HIP 61534 as our calibration star. It has a V-band magnitude of 8.88 and was determined to be close enough to both the target galaxies to have similar levels of atmospheric extinction.



(a) NGC 4145

(b) NGC 4151

Figure 1: Colored images of the two targets we generated using CCDStack and Photoshop. The quality of images is not great, due a number of factors discussed later in the paper.

3 Data: Collection and Processing

3.1 Data Collection

We wish to observe our targets in all available filters — the broadband filters LRGB and the narrowband filters H α , [OIII], and [SII]. The broadband images would inform us of the brightness of the object in different wavelength ranges in the visible spectrum, and would allow us to compare the color of the central bright object in the Seyfert to other features in both galaxies. The narrowband images would allow us to detect spectral lines in different regions in the galaxies, if any.

3.1.1 Determining Exposure Times

We wish to obtain two sets of data for each object in the broadband filters — one set with short exposure times to image the galactic centers only, and one set with long exposure times to image the arms of the galaxies as well. For the narrowband filters, we wish to take long exposures only. For all the long-exposure images, we aim to be able achieve a signal-to-noise ratio of 5 for objects with a magnitude 23 in the arms of our galaxies, such that we can just claim a detection. We decided to take 4 sets of 60s exposures in all broadband filters for both galaxies, and we determined that the desired signal-to-noise ratio would be reached if we took 300s exposures in all filters — 2 each in the L and B bands, 4 in the G-band, and 6 in the R band. We found out, however, that the number of exposures required for the narrowband filters was extremely large — 350x300s exposures in [OIII], 2100x300s in H α , and 1300x300s in [SII]. Given that we only have one night for observations, taking these many exposures is impossible. Therefore, we decide to take as many exposures in the narrowband filters as our longest broadband filter, which is R.

For our calibration star, we are simply interested in converting the signal in DNs to physical flux units, so we decide to take 4x20s exposures in all filters to get a good signal-to-noise ratio without overexposing the star.

3.1.2 Observing at the Telescope

We conducted observations at the C.E.K. Mees Observatory remotely from the River Campus at the University of Rochester on the night of March 22-23, 2021. Due to technical difficulties, we started our observations later in the night at 10:23 PM (March 23 02:23 UTC). The temperature at the observatory was 51.5°F, with 5-10 mph winds and 25% humidity. The skies were clear, but it was expected to get progressively cloudier past midnight.

Typically, a night of observation begins with taking flat field images in all filters to map the dust pattern on the camera, but due to technical issues we cannot do that remotely. So, we straightaway start up the telescope, initialize its position at zenith, and set the equatorial track rate to 15.02 arcsec/sec. Next, we focus the telescope using the following equation:

$$f = 18.4T[F] + 2250 \quad (1)$$

where $T[F]$ is the current temperature in Fahrenheit. Therefore, we moved the focus position of the telescope from 4000 to 3197.

We then connect the telescope to the software TheSky, which is used to slew the telescope to a desired target in the sky. We then initialize the telescope pointing by selecting a bright star near zenith (Talitha; V-magnitude 3.20) and taking a short exposure image in the Luminance filter (L-band) with 2x2 binning. We identify the star in the frame and adjust the telescope offset to ensure the target lies in the center of the frame when we take the next image. We then determine the atmospheric seeing, or the amount by which an image is distorted due to atmospheric scintillation. We slew to a dim star near zenith (GSC 2989-966, V-magnitude 12) and took a 30s exposure in L using 2x2 binning. We obtain a half-flux diameter, or the full-width-half-maximum (FWHM) of the signal, to be 5.57 arcsec. The seeing is computed by multiplying the FWHM by 0.448, which gives us 2.5 arcsec.

With the telescope properly set up, we slew to the calibration star HIP 61534. As determined earlier, we take 4x20s exposures in all filters, using 1x1 binning in L and 2x2 binning for all the others. As the CCD camera takes images of our target, the FIT files containing the data are saved to disk. The header of each file contains information about the filter used, the binning, the time the image was taken at, and the altitude of the object.

Next, we slew the telescope to our Seyfert galaxy, NGC 4151. Since our maximum exposure time is 300s, we decide to set up the telescope's Autoguider. We identify a guide star, GSC 3017-807, (V-magnitude 12.51), that is located in the telescope's Autoguider periphery. We set the telescope to take 60s exposures of this star in the L band with 1x1 binning until aborted, so that it can continue to point towards the same object in the sky and keep our target in the frame. We then set up the telescope to take a series of consecutive exposures in all the filters as determined in an earlier section, choosing 1x1 binning in L and 2x2 in the rest. We wait till all the images are captured while observing the Autoguider window, ensuring that the autoguiding star does not exit the frame.

Once all the series of images are completed, we slew back to our calibration star HIP 61534, and repeat the same steps as before to take another set of 4x60s exposures in all filters. After its completion, we move to the final target, NGC 4145. Once again we set up the Autoguider using consecutive 60s exposures of GSC 3017:869 (V-magnitude 12.42) in the L band using 1x1 binning. Just like in NGC 4151, we set up a series of exposures as determined before using 1x1 binning in L and 2x2 in all other filters. While the camera captures images of our target, we keep an eye on the Autoguider window to ensure that the star remains in place.

After we are done collecting data for the night, we disconnect the telescope from TheSky software, stow the mount at zenith, and close the dome. We log information about the weather, seeing, internet speeds, and all technical issues we faced throughout the night into the Mees Observing Logs.

While imaging NGC 4151, we notice that the background is extremely bright, and determined that it was possibly due to the full Moon nearby. Additionally, we also noted the poor quality of our images for NGC 4145. Prof. Douglass reported seeing haze at the Observatory, which could be a contributing factor.

3.2 Data Reduction

Before we can analyze our targets, we need to perform a series of steps that reduce the signal-to-noise of our images and correct for any transients. These steps comprise the data reduction process. Data reduction is carried out separately for each filter and exposure length for a given target.

The very first step is to calibrate our images using Master dark and bias fields in their respective binning, which subtract the effects of dark and bias current from our frames. To do so, we use the

software CCDStack. For each target, we open the long-exposure L images together, and apply the 1x1 binning Master bias and dark subtraction to all images in this stack. Since we did not take flats on our night of observation, we used Master flat fields in L generated on March 30, 2021 and discovered that the dust patterns matched well. Additionally, we removed all hot and cold pixels in the images. Then, we aligned all images in the stack using a Bicubic B-Spline. All steps described here are repeated for the remaining filters, but using 2x2 binned master fields instead.

Since all our images are taken at different altitudes, the light from the target passes through different levels of the atmosphere. Since the atmosphere becomes thicker as we move from zenith to the horizon, we expect the flux to decrease with decreasing altitude. Therefore, we need to correct for the effects of atmospheric extinction by bringing all images in the stack to the same zenith angle. The first part of this correction process is performed in CCDStack — we select the image in the stack that was closest to zenith and select the background and highlight areas. CCDStack "normalizes" the remaining images in the stack to the reference image such that the flux of the highlighted area in all images is no longer a function of the altitude.

The second part of this process is to correct the fluxes in all images as if they were all taken at zenith. This allows us to compare images across all filters uniformly and with minimal atmospheric extinction. To do so, we scalar multiply all our normalized images by the factor $1 - \sec z_0 \cdot \tau_0$, where z_0 is the zenith angle of the reference image used for normalizing in CCDStack and τ_0 is zenith optical depth of the filter. To find τ_0 , we plot the signal of a reference star in the frame as a function of $\sec z$, where z is the zenith angle of that object in that frame. To find its signal, we use the software ATV, which is a part of the IDL software package. ATV allows us to open a FITS image file and study the photometry of any object in the frame. In the "ImExam" mode, we click on a reference star that is neither too bright nor too dim, which opens up a Photometry window centered on it. We adjust the aperture radius such that it contains the entire signal from the star, and adjust the inner and outer sky radii to define the background annulus. ATV also calculates the photometric error in the signal using the CCD gain ($1.35 \text{ e}^{-1}/\text{DN}$) and the readout noise (9 e^{-1}), and the FWHM which can be multiplied by 0.224 to find the seeing in 1x1 binning and by 0.448 in 2x2 binning. We then plot this signal in DNs as a function of $\sec z$ for each filter and exposure length separately. Theoretically, we would expect a decreasing linear trend of the form:

$$\text{signal} = -\tau_0 f_0(\sec z) + f_0 \quad (2)$$

where f_0 is the absorption-corrected flux density. We fit a linear trendline to our signal vs $\sec z$ plots and calculate f_0 and τ_0 for the given filter.

We note, however, that our FWHM values are extremely large after the first 15 images, which means that the seeing became extremely bad as the night progressed; the maximum value of the seeing we obtain is about 5 arcsec. Therefore, we have some inconsistencies with our signal vs $\sec z$ plots, as seen in Fig. 2. So, even as our objects continued to rise closer to zenith, the quality of our images kept worsening. Since the seeing remained variable all night, we did not get reasonable trends in our most of data, and certainly could not use negative values of f_0 and τ_0 for our analysis.

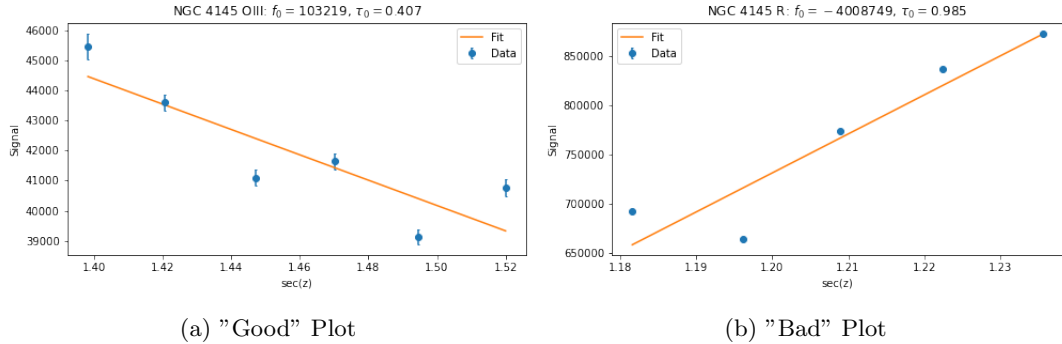


Figure 2: Two examples of signal vs $\sec z$ plots. In (a), the flux decreases as a function of $\sec z$ as expected; however, in (b) it ends up increased. Unfortunately, most of our data resembled plot (b), even some with $\tau_{\text{au}} < 0$.

As a compromise, we decide to take the absolute value of τ_0 from our fitted trendline and use that in our scalar multiplication factor. This corrected our images for atmospheric extinction to the extent that was possible given the poor quality of our data.

The final step in this part of the data reduction is to open our atmosphere-corrected images once again in CCDStack, apply a Poisson sigma correction to remove transients, and generate a mean image for each filter in each exposure time. Averaging the images increases the signal-to-noise ratio in the final image.

However, each pixel in our mean image contains a signal value in DNs, which we wish to convert to physical flux units (erg/s/cm^2) for further analysis. This is where our calibration star comes into play. We first scalar divide the mean images of the two galaxies by the exposure time, such that the value contained in each pixel is in units DN/s. Then, we scalar multiply these images by the following factor for each filter:

$$f_{\text{filter}} = \frac{F_{\lambda_0} \lambda_0 \Delta \lambda}{s_{\text{cal}}} \quad (3)$$

where F_{λ_0} is the flux density of the A0V star in the given filter, λ_0 is the central wavelength, $\Delta \lambda$ is the bandwidth, and s_{cal} is the signal of the calibration star measured in DN/s. The values of F_{λ_0} , λ_0 , and $\Delta \lambda$ have been taken from (cite lecture slide, Lecture 3 slide 11). Since F_{λ_0} is defined for a zero magnitude star, we multiply it by $10^{-8.88/2.5}$ to scale it to our 8.88 magnitude calibration star. Typically, A0V stars have strong absorption features in H α , and we would have to use a different star in the frame calibrate our H α galaxy images. However, we note that due to the poor signal-to-noise ratio in our H α images and bad seeing during the observations, the brightest star in our frame still remains the calibration star. So, even though this would likely not give us a good conversion into physical flux units, we are still forced to use this star for our H α conversions as well.

The signal of the calibration star s_{cal} has some uncertainty σ_s associated with it, which is reported as the standard deviation of the signal measured in all our processed images in a given filter. Since the conversion factor f_{filter} depends on the signal of the calibration star, each pixel in the new flux-converted image will have the following error associated with it:

$$\sigma_f = \left| \sigma_s \frac{d}{ds_{\text{cal}}} f_{\text{filter}} \right| = \frac{\sigma_s}{s_{\text{cal}}^2} \quad (4)$$

which follows from the standard error propagation formula.

We also convert our images from DN/s to magnitude units. To do so, we use the following equation:

$$M = m + 2.5 \log_{10} \frac{f}{\text{signal}} \quad (5)$$

where m is the magnitude of the calibration star, f is the flux of the calibration star in DN/s, and signal is the value contained in each pixel in DN/s. The uncertainty is this value for each pixel is also given by the standard error propagation formula described in Eq. 4.

4 Analysis

Before we proceed further, we need to confirm whether our desired magnitude limit is reached, i.e. if we get a high enough signal-to-noise ratio to claim a detection in a 23-magnitude region. To check this, we open the magnitude-converted images in CCDStack and identify 23-magnitude regions in our galaxy arms. We open these images again in ATV and measure the signal-to-noise ratio of the identified regions. As per our experimental design, we wish to obtain a signal-to-noise ratio of at least 5 in these regions to claim a detection. We found that this limit was reached for all our broadband images for both galaxies, but none of our narrowband images in either galaxy. This is because as mentioned in Table x, the number of exposures required to reach the desired signal-to-noise ratio in the narrowband images far exceeded the amount of time we had to collect the data at the telescope. However, we should still be able to carry out meaningful analyses and compare the salient features of the two galaxies we have imaged.

4.1 Analyzing the Bulges and Star Formation Regions

As evident in Fig. 1, NGC 4151 has a bright central object, while NGC 4145 has no such counterpart. This is further evidenced by our 60s exposures in the L-band, as shown in Fig. 3.

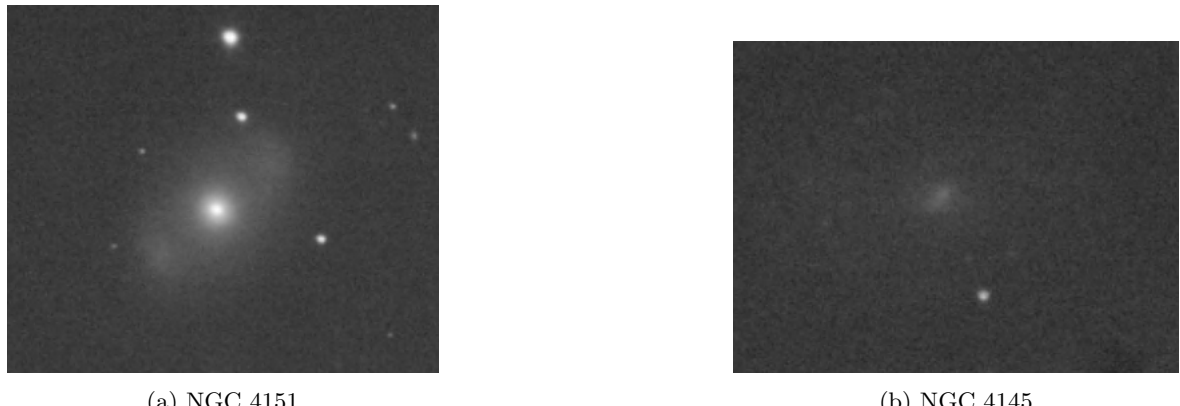


Figure 3: 60s exposures in the L-band, 1x1 binning, averaged. Clearly, a bright, star-like object dominated the center of the Seyfert NGC 4151 which has no counterpart in NGC 4145.

However, both galaxies have clear bulges in their centers, as seen in Fig. x (for NGC 4151 this lies outside the central bright mass). We do note that according to the galaxies' Hubble classification types (cite), NGC 4145 has a larger bulge than NGC 4151. While this makes direct comparisons of the brightness and color a bit trickier, the Seyfert having a smaller bulge makes it slightly easier to compare the color profiles of the two bulges, because the extra brightness from the nucleus is still concentrated in a smaller region. Additionally, we are able to detect some HII regions in both galaxies, as marked in Fig. 4.



Figure 4: Some large star-formation regions as seen in the 300s L-band images for both galaxies, 1x1 binning, averaged. Hereafter, the regions circled in green shall be referred to as "HII Region 1" in the report for each galaxy, and regions circled in red shall be referred to as "HII Region 2".

We first study the magnitude profiles of the centers and large star formation regions of both galaxies. We plot the magnitude in the G-band as a function of the pixel distance from the center of the region of interest. Fig. 5 shows this plot for the central regions of the two galaxies.

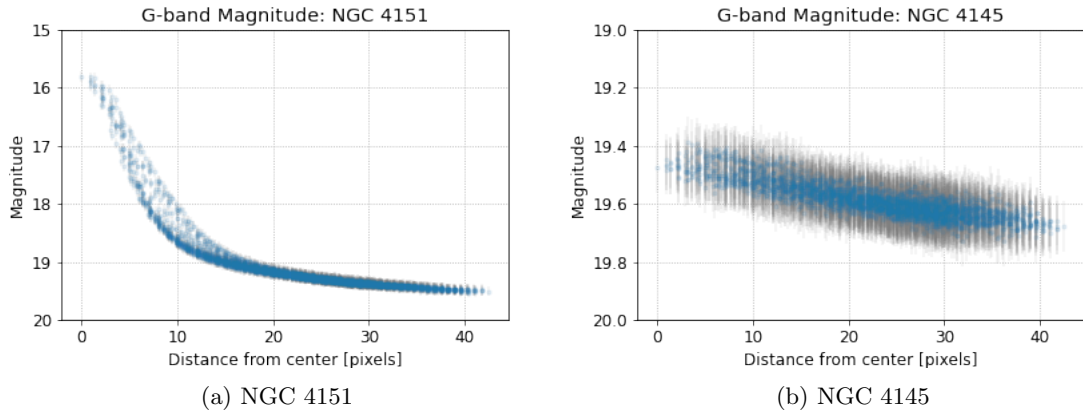


Figure 5: G-band magnitudes for the two galaxies as a function of the pixel distance from the galactic centers.

The G-band filter has properties similar to the Johnson V-band, which gives us an estimate of the brightness of an object. As expected, there is a large variation in the brightness of the Seyfert galaxy NGC 4151 due to presence of a bright object in its center. However, the G-band magnitude falls off rapidly as a function of the pixel distance, which indicates that the brightness is concentrated in a very small region. After a distance of about 15 pixels from the center, the magnitude only shows a very slight downward trend. On the other hand, the reference galaxy NGC 4145 has only a slight downward trend in its G-band magnitude profile throughout its central bulge. Since the galaxies are located at similar distances away from Earth, the values of the G-band magnitudes are very similar outside the central region of the Seyfert.

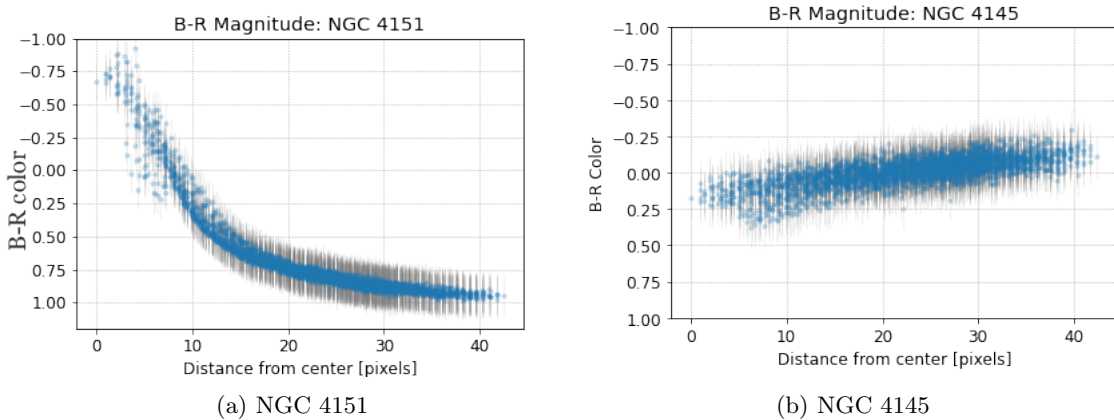


Figure 6

We can further plot the B-R color index for the centers of the two galaxies as a function of pixel distance, as shown in Fig. 6. Once again, there is a large variation in the color of the center of NGC 4151. The center is itself very blue, but becomes progressively redder as a function of pixel distance. This points to the possibility of the presence of a young stellar population at the center; the likelihood of this scenario is discussed in later sections. Furthermore, the the bulge is quite red, which indicates an ageing stellar population. The B-R color index for NGC 4145 is, however, peculiar. It is slightly red at the center which would indicate the presence of older stars, but becomes more and more blue as a function of pixel distance, which indicates that the center is surrounded by a young population. However, this variation is not much, and the B-R color index is approximately zero throughout within one standard deviation. Also note that the images for NGC 4145 are of poor quality due to the extremely high seeing we encountered on the day of observation, which has likely affected the quality of our data. These possible inaccuracies in our raw data may have propagated through to our magnitude-converted images.

The same magnitude profiles can also be generated for HII regions spotted in the galaxies (marked in Fig. 4). These figures can be found in the Appendix.

We can also compute and compare other color indices for the central object and bulge of the Seyfert galaxy, the bulge of the reference galaxy, and some star formation regions in both galaxies. Since color is related to the ratio of the fluxes measured in two filters, we find the flux contained in the regions of interest using our flux-converted images. In ATV, we select an aperture radius that contains our region of interest, carefully define and inner and outer sky radii such that they lie outside the galactic arms, and compute the associated photometric errors. We then take the ratio of fluxes obtained from two broadband images, and compute the uncertainty in that measurement by adding the photometric errors and the uncertainty in the conversion factor (Eq. 4) in quadrature for each pixel in the aperture radius. These values have been tabulated below.

Object and Region	B/R	G/R	B/G
NGC4151, Center	1.86 ± 0.01	0.94 ± 0.01	1.98 ± 0.01
NGC4151, Bulge	1.46 ± 0.01	0.93 ± 0.01	1.00 ± 0.01
NGC4151, HII Region 2	1.41 ± 0.16	0.81 ± 0.10	1.73 ± 0.20
NGC4145, Bulge	0.20 ± 0.01	0.34 ± 0.01	0.40 ± 0.01
NGC4145, HII Region 1	0.37 ± 0.01	0.44 ± 0.01	0.84 ± 0.02

Table 1: Ratios of broadband fluxes (colors)

We note that the bulge of NGC 4151 is much brighter than the bulge of NGC 4145 in the G-band,

which is consistent with our plots in Fig. 5. Interestingly, and contradicting our earlier plots in Fig. 6, the bulge of NGC 4145 is extremely red, which is in stark contrast with the extremely blue bulge of NGC 4151. Once again, this is likely because of poor quality of raw data. We note that the raw images for NGC 4145 captured in the R-band had a much better signal-to-noise ratio, we choose to believe the flux ratios calculated in Table 1. It does seem more likely that the bulge of NGC 4145 has an ageing stellar population, while both the bulge and center of NGC 4151 are very blue and seem to have younger stellar populations. Although it seems like that B/R ratio for the NGC 4151 bulge is high due to a relatively lower R-band flux, rather than an abundance of B-band flux, since the B/G ratio is 1. The center, however, seems to be dominated by emissions in the B-band.

We also get conflicting results for the HII regions in both galaxies. The HII region identified in the Seyfert is markedly blue. This would usually be expected from a young stellar population, but a strong $H\alpha$ emission line contained in the R-band would typically make a star formation region look red instead. We discuss later in the section how we could not visually see any star formation regions in disk of NGC 4151 in the $H\alpha$ images, which likely points to a poor signal-to-noise ratio in $H\alpha$. Since the R-band image did not pick up any flux from $H\alpha$, the star formation regions in NGC 4151 look blue. Their color indices are very similar to the central object in the Seyfert; however, the main difference is that the central object shows up very clearly in the $H\alpha$ images, which means that its flux does get included in the R-band flux. This implies that the center of the Seyfert is bluer than its star formation regions. On the other hand, the star formation regions in NGC 4145 are very red as we would expect; the arms of the galaxy have a good signal-to-noise ratio in the R-band images, and the star formation regions are visible in the $H\alpha$ images as well. Therefore, the R-band flux dominates, and the central object in the Seyfert remains the bluest region we observed so far in both galaxies.

4.2 Spectral Analysis of the Center

Another basis of comparison between the centers and star formation regions of the two galaxies is the similarities or differences in their absorption and/or emission spectra. This can be done by comparing the fraction of broadband fluxes contained in the narrowband images for the central object and galactic bulges, and comparing them to the fractions we would expect from a continuum source. We illustrate this methodology using Fig. 7.

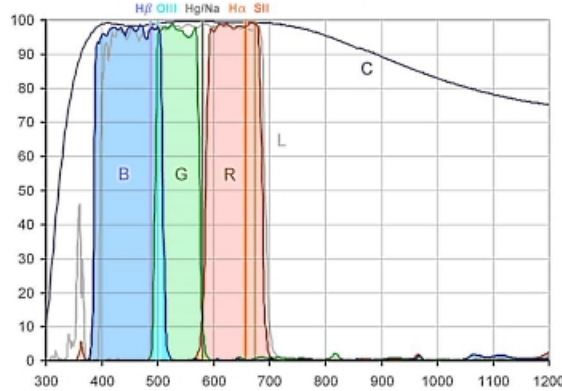


Figure 7: Caption (cite)

The wavelength of the [OIII] band is entirely contained in both the B and G bands, which means that the flux measured in both B and G bands includes some [OIII] emissions. Similarly, the flux measured in the R band includes the measurements in the $H\alpha$ and [SII] bands. For a continuum source such as the one depicted in Fig. 7, the fraction of the broadband fluxes contained in the narrowband images would simply be the ratio of their bandwidths. We compare these bandwidth ratios to the flux ratios [OIII]/B, [OIII]/G, and ($H\alpha$ +[SII])/R for the central object and bulge of NGC 4151, and the

bulge and star formation regions of NGC 4145. If the flux ratios are greater than those expected from a continuum source, we can say that the object as an emission line in that wavelength. A compilation of these fractions is depicted in Table 2.

However, due to poor signal-to-noise ratio in our narrowband images, we were not able to see any structure to the arms of the Seyfert NGC 4151, and therefore could not visually detect any star formation regions. Similarly, for NGC 4145, we cannot claim a measurement on our fluxes for the star formation regions. We can therefore only compute upper bounds on our flux measurements; the fractions shown in Table 2 have been computed from those upper limits. Therefore, these values should be taken at face value, and may not give us results that are comparable to expectations. Better observing conditions and more number of exposures would have helped us reduce the noise in our signal and possibly obtain more reasonable values for the fluxes.

Object and Region	[OIII]/B	[OIII]/G	(H α +[SII])/R
Continuum Source	0.066	0.106	0.149
NGC4151, Center	0.077 \pm 0.001	0.154 \pm 0.001	0.719 \pm 0.002
NGC4151, Bulge	0.062 \pm 0.008	0.097 \pm 0.013	0.406 \pm 0.008
NGC4145, Bulge	0.194 \pm 0.107	0.077 \pm 0.023	0.123 \pm 0.020
NGC4145, HII Region 1	<0.134	<0.112	<0.167

Table 2: Fraction of broadband fluxes contained in the narrowband images, for different objects in the two galaxies. The expected flux ratios for a continuum source have also been included for comparison. Note that no star formation regions were observed in the narrowband images of NGC 4151.

We see that the central object in the Seyfert NGC 4151 has a weak emission line in [OIII], as evidenced by the only slightly higher flux ratios as compared to a continuum source. In comparison, the bulge of NGC 4151 does not seem to have any emission feature in [OIII] — the [OIII] bandwidth ratios for the continuum source lie within one standard deviation of the measured flux ratios. The same applies to the bulge of NGC 4145, for which we do not detect an emission line in [OIII]. The upper bounds computed on the [OIII] flux ratios for the star formation region in NGC 4145 agrees with a weak [OIII] emission line, which is consistent with hot young stars in an HII region.

We also see that the central object in NGC 4151 has an extremely large emission line in H α +[SII]. If we split the two spectral lines, we find that the majority of the contribution to this increased flux is due to H α , while [SII] is comparable to the continuum flux ratio. In the earlier section, we saw that the center of NGC 4151 was very blue; this means that the R-band flux in the center is by itself extremely low and completely dominated by the spectral line in H α . The bulge, too, has a much larger fraction of the R-band flux as a result of H α and [SII]; once again, the flux ratio for [SII] is consistent with a continuum source and there is a clear emission line detection in H α . However, the fraction of the R-band flux contained in H α and [SII] is much larger for the central object than for the bulge. On the other hand, the bulge of NGC 4145 does not show any emission line in H α or [SII] as its flux ratio is within one standard deviation of the continuum bandwidth. The upper bound on the H α and [SII] flux for the star formation region is consistent with a weak emission line in H α .

Therefore, the data so far indicates that the central object in NGC 4151 may have signs star formation.

4.3 Analyzing the central object

The compact central object in NGC 4151 is of the greatest interest to this analysis, and we now wish to verify the source of this brightness by computing its luminosity. The luminosity L is given by:

$$L = 4\pi fr^2 \quad (6)$$

where f is the flux of the central object as measured in AT8 from our flux-converted images in the L-band, and r is the distance of the center of the galaxy from Earth (15.8 ± 0.4 Mpc). Carrying out

the necessary unit conversions and plugging in the known values we obtain:

$$L_{\text{center}} = (3.10 \pm 0.16) \times 10^9 L_{\odot} \quad (7)$$

This is an extremely large luminosity. Comparing this to the luminosity of the galaxy, we discover that the galaxy is responsible for $\left(\frac{f_{\text{center}}}{f_{\text{galaxy}}}\right)^2 \approx 25\%$ of the luminosity of the entire galaxy.

One also notes that this luminosity originates from a very small area within the galaxy. Using the photometry tool in ATV, we obtain that the central region has a diameter of 13 pixels in the L-band images which were taken with a 1x1 binning. In this binning, the image obtained has dimensions 4096x4096 pixels; since the CCD camera's field of view is 15.4 arcminutes, each pixel corresponds to 0.225 arcseconds in the sky, or one arcsecond is spanned by roughly 4 pixels in the image. The average seeing at the time of taking the L-band images of NGC 4151 was roughly 2.7 arcseconds, which corresponds to 12 pixels. We assume that the uncertainty in our measurement of the pixel diameter was half of the seeing i.e. 6 pixels. Therefore, the pixel diameter corresponds to an angle $\theta = 2.93pm1.35$ arcseconds subtended in the sky by the central object. This can be converted into a physical distance d using the known distance r to the galaxy:

$$d = \theta \cdot r = (224 \pm 104)\text{pc} \quad (8)$$

where the uncertainty in the distance has been computed by propagating the uncertainties in θ and r . Clearly there is a very large uncertainty range in our measured value of the diameter of the central object of NGC 4151 due to the large values of seeing we had on our night.

5 Discussion: Determining the Nature of Central Object in NGC 4151

While we know a priori that NGC 4151 is a Type 1.5 Seyfert with an actively accreting black hole, we wish to explicitly rule out other explanations for the bright region that we see in our images. In this section, we consider some possible hypotheses and determine if they can be ruled out based on our analyses so far.

5.1 Stellar Cluster

One possible explanation for the source of the central luminosity is a massive stellar cluster conveniently located at the center of the galaxy. For ease of calculation, we shall assume that all stars in this hypothetical giant cluster are main sequence stars.

To see if this is a possibility, we use the stellar mass function (Fig. 8). The stellar mass function describes the relative distribution of stars in a typical stellar population as a function of the mass of the stars. For example, Fig. 8 suggests that for each $11 M_{\odot}$ star in a typical stellar population, there are $10^5 8 M_{\odot}$ stars. Therefore, the total number of stars in a typical cluster would simply be the area under this curve.

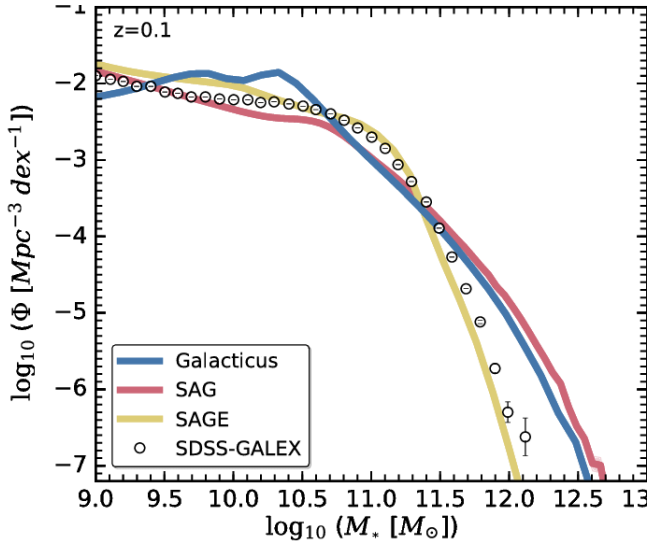


Figure 8: Stellar mass function, taken from Rodriguez et al. [5]

A simple way of determining the area under the stellar mass function is to instead use the initial mass function, which is an empirical relation written in a functional form and therefore is easier to integrate. The initial mass function describes the initial distribution of masses for a population of stars, and yields a shape similar to that of the stellar mass function. Given the broad assumptions we make regarding the composition of our hypothetical stellar cluster, it is a reasonable approximation to use area under the initial mass function to describe the total mass of a typical stellar cluster.

The initial mass function takes on different forms, and is usually stated in its logarithmic form; in this analysis, we shall use the Kroupa equation which is given by [1]:

$$\xi(m) = m^{-\alpha} \quad (9)$$

where α is a dimensionless constant which takes on the following values:

$$\alpha = \begin{cases} 0.3 & m < 0.08M_\odot \\ 1.3 & 0.08M_\odot < m < 0.5M_\odot \\ 2.3 & m > 0.5M_\odot \end{cases} \quad (10)$$

The mass of a stellar cluster is then the integral of this function; that is,

$$M_{\text{total}} = \int_{M_{\text{min}}}^{M_{\text{max}}} \xi(m) dm \quad (11)$$

Since it is rare to find stars with a mass less than $0.1 M_\odot$, we shall use $M_{\text{min}} = 0.08M_\odot$ as the lower bound in our integral, thus making it easier to directly use Kroupa's initial mass function. Also, following the maximum mass limit in the stellar mass function depicted in Fig x, we choose $M_{\text{max}} = 11M_\odot$. Therefore, performing the integral in Eq. 11 and exponentiating the result gives us the total mass contained in a typical stellar population:

$$M_{\text{total}} \approx 7.4 \times 10^5 M_\odot \quad (12)$$

Furthermore, we can determine the luminosity of a typical cluster by converting the masses of the stars on the x-axis of the stellar mass function into luminosities. The mass-luminosity relation is given

by the following equation [6]:

$$\frac{L}{L_\odot} = \begin{cases} 0.23 \left(\frac{M}{M_\odot}\right)^{2.3} & M < 0.5M_\odot \\ \left(\frac{M}{M_\odot}\right)^4 & 0.5M_\odot < M < 2M_\odot \\ 1.4 \left(\frac{M}{M_\odot}\right)^{3.5} & M > 2M_\odot \end{cases} \quad (13)$$

Eq. 11 can be transformed into an integral in the luminosity L instead of mass m , and the result of the integration will be the luminosity of this particular cluster. This computation yields us:

$$L_{\text{total}} \approx 9.2 \times 10^8 L_\odot \quad (14)$$

In Eq. 7, we calculated the luminosity of our central object in NGC 4151 to be $3.1 \times 10^9 L_\odot$, or about 3.4 times the luminosity of the stellar cluster considered in this example. Accordingly we can scale the mass of this cluster by the same factor to find the total mass of our hypothetical central cluster; that is, if the central luminosity of NGC 4151 originated from a giant stellar population, it would have mass $2.5 \times 10^6 M_\odot$. The Schwarzschild radius of this mass is much smaller than the diameter of the central object we measured in Eq. 8. So in principle, it is possible to fit these many stars into a very small area without triggering a gravitational collapse. However, it is still highly unlikely that this is a stellar cluster, purely because these many stars in an area like this would ultimately collide with each other, and the center would not be stable. Also, we found earlier that the center of the Seyfert was extremely blue, which means that any hypothetical stellar population it has must be extremely young. But large O-type stars have very short lifespans, and it would be highly improbable for them to sustain in a galaxy especially in such close proximity. Additionally, most stellar clusters which are this massive have old stellar populations, which is not supported by our data. Therefore, we can reject this hypothesis.

5.2 HII Region

Another possible explanation for the origin of the central object could be a giant HII region. In earlier sections, we described the differences in the color of the central object and star formation regions in both galaxies, and found certain similarities, but the one stark difference was that the central object was much bluer than a typical HII region. If we assume that the center is indeed an HII region, the large blue flux can only be explained by the presence of young, hot O-type stars, but as we saw in the earlier section this seems improbable due to the compactness of the central object.

Another way to see if this is a possibility is by calculating the relative abundances of doubly ionized oxygen and singly ionized sulfur in the center of NGC 4151, and compare it to the known values of the relative abundances for a typical HII region.

In Table 2, we computed the flux ratios $[\text{OIII}]/\text{H}\alpha$ and $[\text{SII}]/\text{H}\alpha$ for the central object along with their associated uncertainties. These values can be used to compute the relative abundances. The relative abundance of doubly ionized oxygen $\chi_{\text{O}^{++}}$ is given by:

$$\chi_{\text{O}^{++}} = \frac{\lambda_{[\text{OIII}]} \alpha_{\text{H}\alpha}}{\lambda_{\text{H}\alpha} \gamma_{[\text{OIII}]}} f_{[\text{OIII}]/\text{H}\alpha} \quad (15)$$

where $\lambda_{[\text{OIII}]} = 5.0068 \times 10^{-5}$ cm and $\lambda_{\text{H}\alpha} = 6.5628 \times 10^{-5}$ cm are the wavelengths of the $[\text{OIII}]$ and $\text{H}\alpha$ transitions respectively, $\alpha_{\text{H}\alpha} = 8.643 \times 10^{-14}$ cm³/s is the effective recombination coefficient of the $\text{H}\alpha$ transition, $\gamma_{[\text{OIII}]} = 1.133 \times 10^{-9}$ cm³/s is the collisional excitation rate coefficient for the $[\text{OIII}]$ transition, and $f_{[\text{OIII}]/\text{H}\alpha}$ is the ratio of the $[\text{OIII}]$ flux to $\text{H}\alpha$ flux at the center from Table 2.

Similarly, the relative abundance for singly ionized sulfur is given by:

$$\chi_{\text{S}^+} = \left(\frac{\lambda_{[\text{SII}]1}}{\gamma_{[\text{SII}]1}} + \frac{\lambda_{[\text{SII}]2}}{\gamma_{[\text{SII}]2}} \right)^{-1} \frac{\alpha_{\text{H}\alpha}}{\lambda_{\text{H}\alpha}} f_{[\text{SII}]/\text{H}\alpha} \quad (16)$$

where $\lambda_{[\text{SII}]} = 6.7308 \times 10^{-5}$ cm and $\lambda_{[\text{SII}]} = 6.7164 \times 10^{-5}$ cm are the wavelengths of the [SII] doublet transition, and $\gamma_{[\text{SII}]} = 6.514 \times 10^{-9}$ cm³/s $\gamma_{[\text{SII}]} = 9.702 \times 10^{-9}$ cm³/s are the collisional excitation rate coefficient for the [SII] doublet.

Plugging in the known values, we obtain that

$$\chi_{\text{O}^{++}} = (1.28 \pm 0.02) \times 10^{-5} \quad (17)$$

$$\chi_{\text{S}^+} = (5.21 \pm 0.08) \times 10^{-7} \quad (18)$$

For a typical HII region, these values are expected to be $\chi_{\text{O},\text{HII}} = (3.3 \pm 0.5) \times 10^{-4}$ and $\chi_{\text{S},\text{HII}} = (1.0 \pm 0.1) \times 10^{-5}$. Clearly, the values we obtain in the above equation are far off from these values, more than 5 standard deviations away. Since our values are atypical for an HII region, we can safely reject this hypothesis.

5.3 Black Hole

With the above two hypotheses being rejected, we can say that it is highly likely that the central object is a third type of object we have not considered yet in this analysis — a supermassive black hole (SMBH). Supermassive black holes are typically found in the centers of galaxies, and have masses of the order of hundreds of thousands of solar masses. To verify whether this luminosity originates from the black hole and its surrounding accretion disk, we first determine its accretion rate using the luminosity found in Eq. 7. We find the accretion rate of the black-hole using the equation [10]:

$$\dot{M} = \frac{12L}{c^2} = 7.95 \times 10^{-11} M_\odot / s \neq 0 \quad (19)$$

Therefore, the central object in our image must be accreting. We know that for an accreting black hole, the limiting mass – called the Eddington mass for a certain luminosity – is given by the equation [10]:

$$M_E = \frac{L_E}{3 \cdot 10^4 L_\odot} M_\odot \quad (20)$$

From our luminosity, we get the Eddington mass to be $M_E \approx 10^5 M_\odot$.

Therefore, for the black-hole to be accreting it must have a mass higher than M_E .

We may also support this hypothesis using the flux ratios calculated in the analysis section in Tables 1 and 2. From our flux calculations, we determined that the center is very blue. If our central object is indeed a black hole with a surrounding accretion disk, this would be consistent because there should be very high energy light coming out of the high-velocity material in the accretion disk. High energy radiations imply that it must be near the blue end of the spectrum. From our analysis we have also found H_α signatures which could also be justified by the accretion disk. Accretion disks can contain dust clouds alongside debris, which may explain the origin of the strong H_α emission lines that we observed.

6 Conclusion

Using the arguments presented in this analysis, we can conclude that it is highly likely that the central object in the Seyfert NGC 4151 is a black hole, with a minimum mass of around $10^5 M_\odot$ and a luminosity of around $10^9 L_\odot$. While this is about 2 orders of magnitude lower than the current estimates of the mass of this SMBH [3], we still were successfully able to calculate a lower limit on the mass using the data obtained in just one night of observation. We also conclude that although the center seems to be blue, it also has a strong emission line in H_α and a weak emission line in [OIII]. The central object is extremely bright, making up for about 25% of the total luminosity of the galaxy, and has no counterpart in the non-Seyfert spiral NGC 4145.

However, our analysis and conclusions were strongly affected by our observational data which was not ideal given the sub-optimal seeing during the observation nights. Our images also had a lot of transients – mostly dust donuts – that were not removed even after flat field subtraction. In addition, our signal-to-noise ratio in the narrowband filters was very poor due to time constraints, as the required number of exposures was very large for a single night of data collection.

We would have had more consistent data that is comparable to previous experiments, had the weather conditions been more conducive to astronomical observations. Larger number of exposures in all filters, but especially in the narrowband filters, would have resulted in a much better signal-to-noise ratio in all our images.

References

- [1] P. Kroupa. “On the variation of the initial mass function”. In: *Monthly Notices of the Royal Astronomical Society* 322.2 (Apr. 2001), pp. 231–246. ISSN: 1365-2966. DOI: 10.1046/j.1365-8711.2001.04022.x. URL: <http://dx.doi.org/10.1046/j.1365-8711.2001.04022.x>.
- [2] Fulvio Melia. “The Galactic Supermassive Black Hole”. In: *Princeton University Press* (2007).
- [3] Christopher A. Onken et al. “THE BLACK HOLE MASS OF NGC 4151. II. STELLAR DYNAMICAL MEASUREMENT FROM NEAR-INFRARED INTEGRAL FIELD SPECTROSCOPY”. In: *The Astrophysical Journal* 791.1 (July 2014), p. 37. ISSN: 1538-4357. DOI: 10.1088/0004-637X/791/1/37. URL: <http://dx.doi.org/10.1088/0004-637X/791/1/37>.
- [4] University of Rochester. *C.E.K. Mees Observatory*. URL: <https://www.sas.rochester.edu/pas/about/observatory.html>.
- [5] Luiz Felipe Rodrigues et al. “Galactic magnetic fields and hierarchical galaxy formation”. In: *Monthly Notices of the Royal Astronomical Society* 450 (May 2015), pp. 3472–3489. DOI: 10.1093/mnras/stv816.
- [6] Maurizio; Santi Cassisi Salaris. “Evolution of stars and stellar populations”. In: (2005), pp. 138–140.
- [7] Carl K. Seyfert. “Nuclear Emission in Spiral Nebulae.” In: 97 (Jan. 1943), p. 28. DOI: 10.1086/144488.
- [8] SIMBAD. *SIMBAD*. URL: <http://simbad.u-strasbg.fr/simbad/sim-basic?Ident=NGC+4151&submit=SIMBAD+search>.
- [9] SIMBAD. *SIMBAD*. URL: <http://simbad.u-strasbg.fr/simbad/sim-basic?Ident=NGC+4145&submit=SIMBAD+search>.
- [10] Ohio State. *Supermassive black holes*. URL: http://www.astronomy.ohio-state.edu/~dhw/A142/notes10.pdf?fbclid=IwAR3whRVeBzdy0tLwnjURdHgZ8CMSM5PLlxooN56IKwX2R5Worz_2H2xQjR4.

7 Appendix

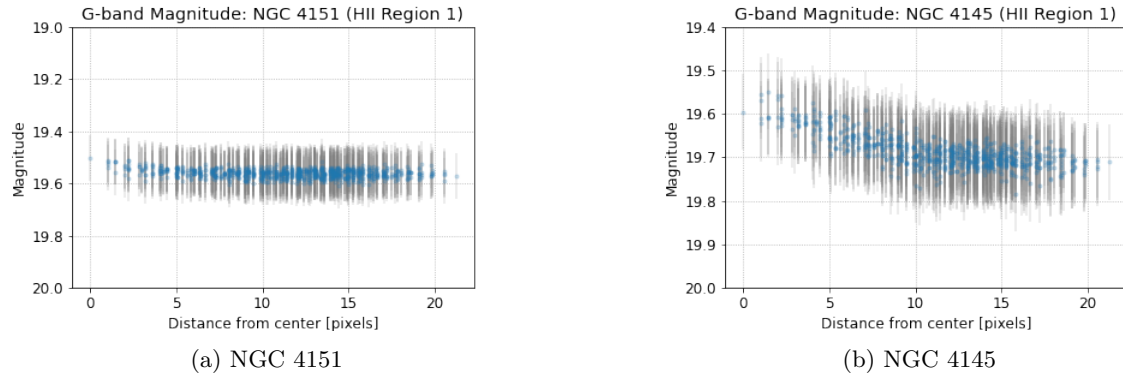


Figure 9: G magnitude as a function of the pixel distance from the center of HII Region 1 (marked in Fig. 4)

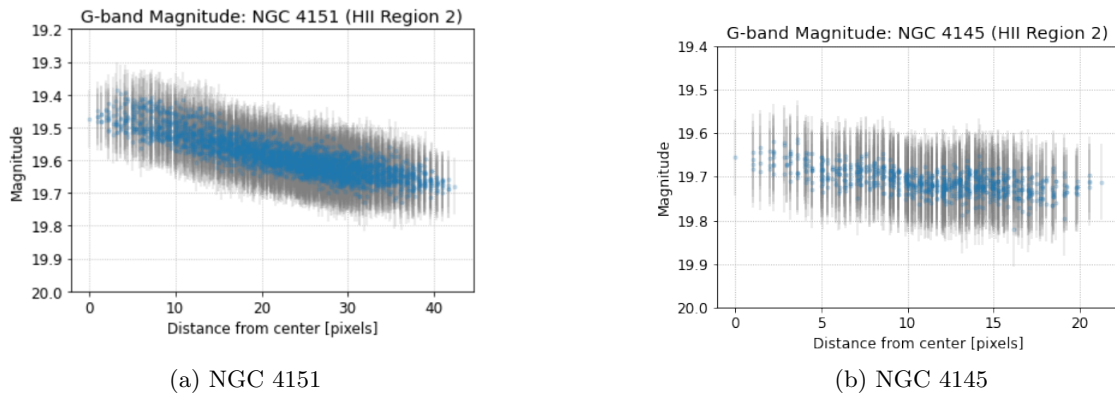


Figure 10: G magnitude as a function of the pixel distance from the center of HII Region 2 (marked in Fig. 4)

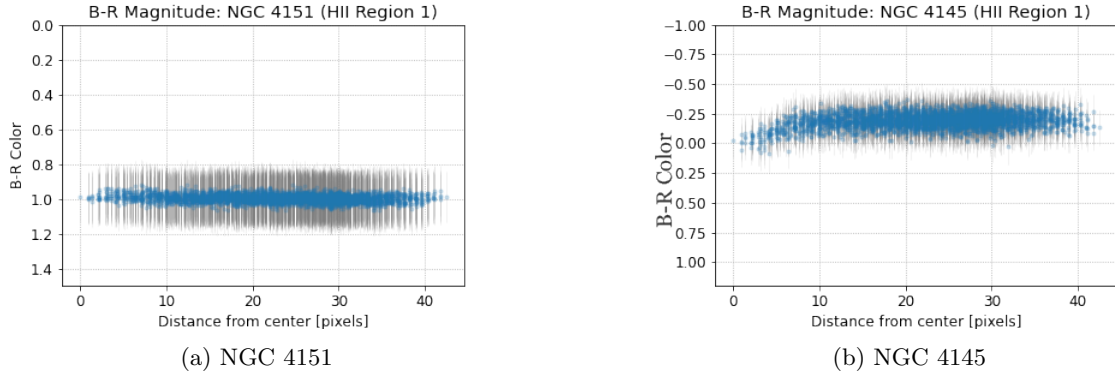


Figure 11: B-R magnitude as a function of the pixel distance from the center of HII Region 1 (marked in Fig. 4)

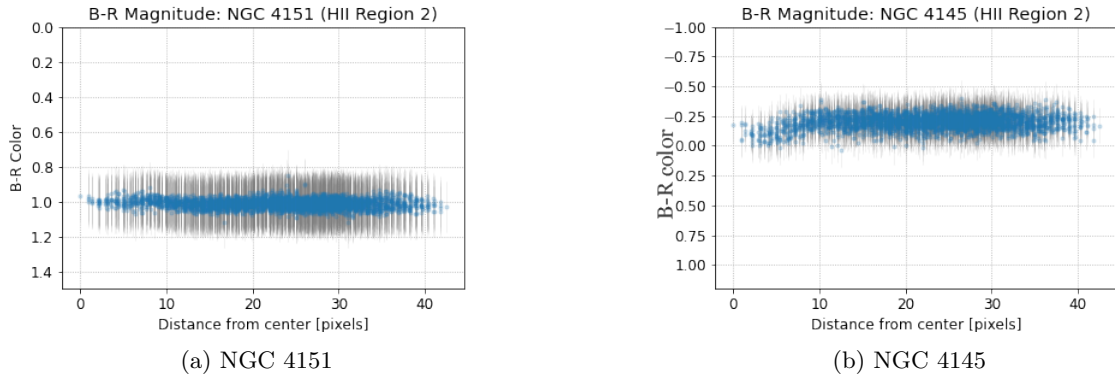


Figure 12: B-R magnitude as a function of the pixel distance from the center of HII Region 2 (marked in Fig. 4)